

# MoS<sub>2</sub> Nanoflakes based Kilohertz Electrochemical Capacitors

Sourayan Bal,<sup>[a]</sup> Rishav Baranwal,<sup>[a]</sup> Xueyan Lin,<sup>[a]</sup> Wenyue Li,<sup>[b]</sup> Shize Yang,<sup>[c]</sup> Nazifah Islam,<sup>[d]</sup> and Zhaoyang Fan<sup>\*[b]</sup>

An ultra-fast electrochemical capacitor (EC) designed for efficient ripple current smoothing was fabricated using vertically oriented MoS<sub>2</sub> (VOM) nanoflakes deposited on freestanding carbonized cellulose (CC) sheets as electrodes. The daily used cellulose tissue sheets were transformed into electrode scaffolds through a rapid pyrolysis process within a preheated furnace, on which VOM nanoflakes were formed in a conventional hydrothermal process. With these ~10 μm thick VOM-CC electrodes, ultrafast ECs with tunable frequency response and

specific capacitance density were fabricated. The ECs with a cell-level areal capacitance density of 0.8 mF/cm<sup>2</sup> at 120 Hz were demonstrated for ripple current filtering from 60 Hz to 60 kHz. At a lower frequency response level, EC cell with a large capacitance density of 4.8 mF/cm<sup>2</sup> was also demonstrated. With the facile and easily scaled up process to producing the nanostructured electrode, the miniaturized VOM-CC based ECs have the potential to substitute the bulky aluminum electrolytic capacitors for current smoothing and pulse power applications.

## Introduction

Aluminum electrolytic capacitors (AECs) are extensively employed for current smoothing in line-frequency AC/DC conversion, high-frequency DC/DC conversion, and pulse power generation. However, they face inherent limitations due to their low capacitance and energy densities. With the miniaturization trend of electronic devices and their power sources, there have been much interest in developing kilohertz high frequency electrochemical capacitors (HF-ECs), with a much higher capacitance density while efficiently responding up to kilo hertz frequencies, in substitution of AECs as filtering capacitors.<sup>[1]</sup> Another potential application of these ultrafast ECs is the bulk decoupling capacitors in voltage regulator modules of electronic devices for noise suppression that typically requires a working frequency up to 100 kHz. These ultrafast ECs may also be used for pulse power generation and harvesting.<sup>[2]</sup>

Conventional ECs or supercapacitors store charges in the double layer formed along the interface between the electrolyte and the electrode. They have often been considered as a viable alternative for bulk batteries<sup>[3]</sup> but not for filtering applications due to a very low operable frequency range. This limitation can primarily be attributed to tortuous pores which are intentionally created to generate high surface area in the electrode since the capacitance is directly proportional to the surface area accessible by ions in the electrolyte. Due to this, the electrolyte ions need to travel a long pathways in these tortuous pores which reduces the response frequency to below 1 Hz range.<sup>[1a]</sup> In contrast, efficient ripple current filtering at line-frequency (60 Hz in the U.S.) requires the capacitor to capacitively respond at 120 Hz and higher harmonic frequencies with minimum resistive loss. Therefore, for ripple current filtering application, the capacitance and the phase angle at 120 Hz, and maximum frequency ( $f_{max}$ ) when the capacitance and the parasitic inductance resonate, are some of the utmost important parameters.<sup>[4]</sup>

Various electrode structures,<sup>[1b,5]</sup> including graphene, carbon nanotube, carbon nanofiber, and other carbon based, as well as other conductive and chemically inert nanomaterials such as conductive polymers, MXene,<sup>[6]</sup> conductive transition metal nitrides,<sup>[7]</sup> 2D transition metal dichalcogenides (TMDCs),<sup>[8]</sup> and many others,<sup>[9]</sup> have been employed to fabricate HF-ECs for ripple filtering. In addition to a very low resistance, these structures typically have a common feature of open pores to strike a balance between capacitance and response frequency.<sup>[10]</sup> Significant progress has been made in this niche area of supercapacitors, including the recent high voltage<sup>[4b,11]</sup> and high capacitance density<sup>[12]</sup> demonstrations.

However, it must be noted that low voltage rated AEC is a very cheap electronic component, less than 10 cents, while most of the reported filtering ECs are based on a delicate nanostructure which might be difficult to be scaled up for high throughput and low-cost production.<sup>[13]</sup> Herein, we report a

[a] S. Bal, R. Baranwal, X. Lin  
School for Engineering of Matter, Transport & Energy  
Arizona State University  
Tempe, Arizona, 85281 (USA)

[b] Dr. W. Li, Prof. Dr. Z. Fan  
School of Electrical, Computer and Energy Engineering  
Arizona State University  
Tempe, AZ 85281 (USA)  
E-mail: zyfan@asu.edu  
Homepage: <https://search.asu.edu/profile/268678>

[c] Dr. S. Yang  
ACEM Core, Yale University  
810 West Campus Drive, West Haven,  
CT 06516 (USA)

[d] Dr. N. Islam  
Edward E. Whitacre Jr. College of Engineering  
Texas Tech University  
Lubbock, TX 79409 (USA)

 Supporting information for this article is available on the WWW under  
<https://doi.org/10.1002/batt.202300363>

new structure and its facile process to produce electrodes of filtering ECs that potentially can be commercialized at a low cost. The electrode structure is based on vertically oriented  $\text{MoS}_2$  (VOM) nanoflakes deposited on carbonized Kimwipe tissue sheets. The daily used cellulose tissue sheets were transformed into electrode scaffolds through a rapid 20-minutes pyrolysis process within a preheated furnace. The obtained carbonized cellulose (CC) fiber scaffold was then used as a substrate to deposit VOM nanoflakes in a conventional hydrothermal reactor. The cost-effectiveness of the device can be seen as cellulose is abundant and extremely cheap, while hydrothermal synthesis is a facile process. With the VOM-CC produced as a freestanding electrode, we demonstrated kHz frequency ECs with high performance. Their application in ac filtering in frequency range from 60 Hz to 60 kHz was demonstrated.

## Results and Discussion

### Electrode material synthesis

The electrode fabrication process is illustrated in Figure 1. Kimwipe cellulose sheets were inserted in a furnace preheated at 1000°C for 20 minutes to achieve rapid carbonization. The carbonized cellulose (CC) sheets were put in a hydrothermal reactor with a mixed solution of sodium molybdate dihydrate and thiourea as the source materials to grow vertically oriented  $\text{MoS}_2$  (VOM) nanoflakes. The hydrothermal reaction was carried out at 220°C for 2–3 hours to control the amount of VOM nanoflakes deposited, which, as will be shown, dramatically impacts the HF-EC performance. These samples are differentiated as VOM-CC-2h for 2 h growth, VOM-CC-2h15m for 2 h 15 min growth, etc. They have a thickness of ~10  $\mu\text{m}$  and can be directly used as freestanding electrodes to assemble ECs.

The carbonization of the cellulose sheets is an important step and has a big effect on the frequency response of the capacitor. Reduction of carbon precursors and partial graphitization can generate inter-connected conductive pathways for effective electron transport. It is known that pyrolysis of cellulose for a long time will improve its conductivity and generate high density micropores, which are beneficiary to conventional ECs, but not preferable for filtering ECs that require high-frequency response. Our previous studies confirmed that a rapid carbonization process with plasma heating is crucial when converting cellulose into carbon fibers for HF-ECs.<sup>[2a]</sup> In this work, we rapidly carbonized Kimwipe tissue sheets in a preheated furnace for 20 minutes.

### Electrode material characterization

The microstructures of CC and VOM-CC were observed using a scanning electron microscopy (SEM). The nonwoven CC (Figure 2a and b) consists of flattened carbonized fiber bundles with different sizes, and the surface of the fiber bundle exhibits wrinkles (Figure S1a in the Supporting Information (SI)). Between these fiber bundles are very large voids of tens of micrometers. For VOM-CC-2h,  $\text{MoS}_2$  was deposited almost uniformly along all the fiber surfaces, and the geometry of the underlying CC scaffold had no obvious change (Figure 2c). At a higher magnification (Figure 2d), intersected  $\text{MoS}_2$  nanoflakes, vertically aligned on the scaffold can be identified. The micrograph in Figure S1(b) in SI further shows sparse nanoflakes wrapped on the CC scaffold with ion readily accessible space between them.

When  $\text{MoS}_2$  hydrothermal growth was expanded from 2 h to 3 h, the morphology of  $\text{MoS}_2$  layer was changed. Instead of a layer of sparse vertical nanoflakes that uniformly wrapped around individual carbon bundles, the nanoflakes became very

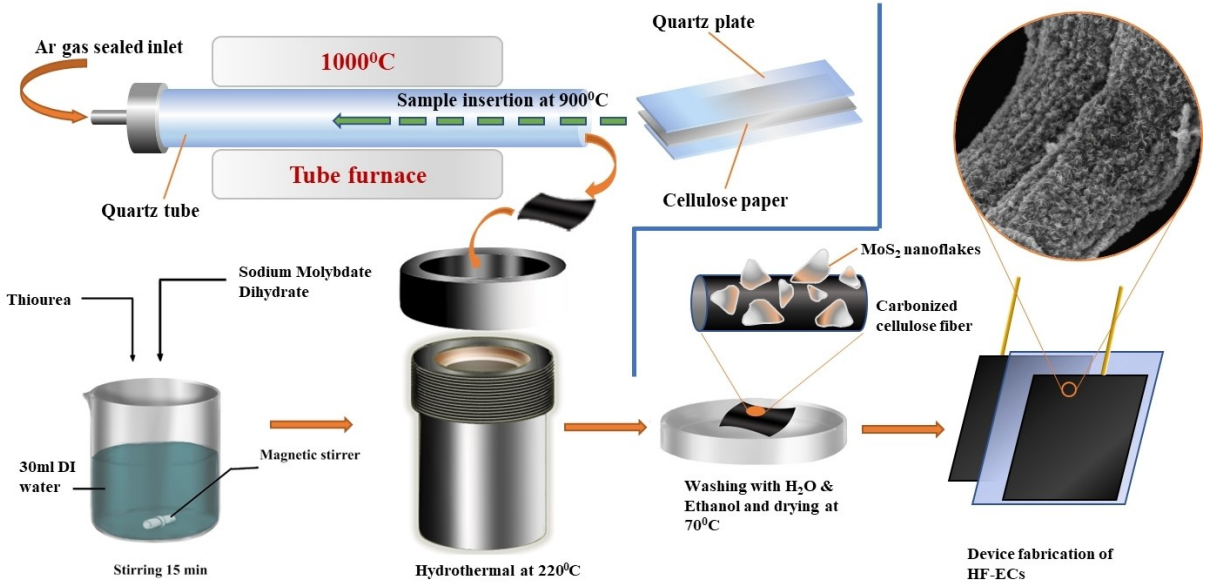
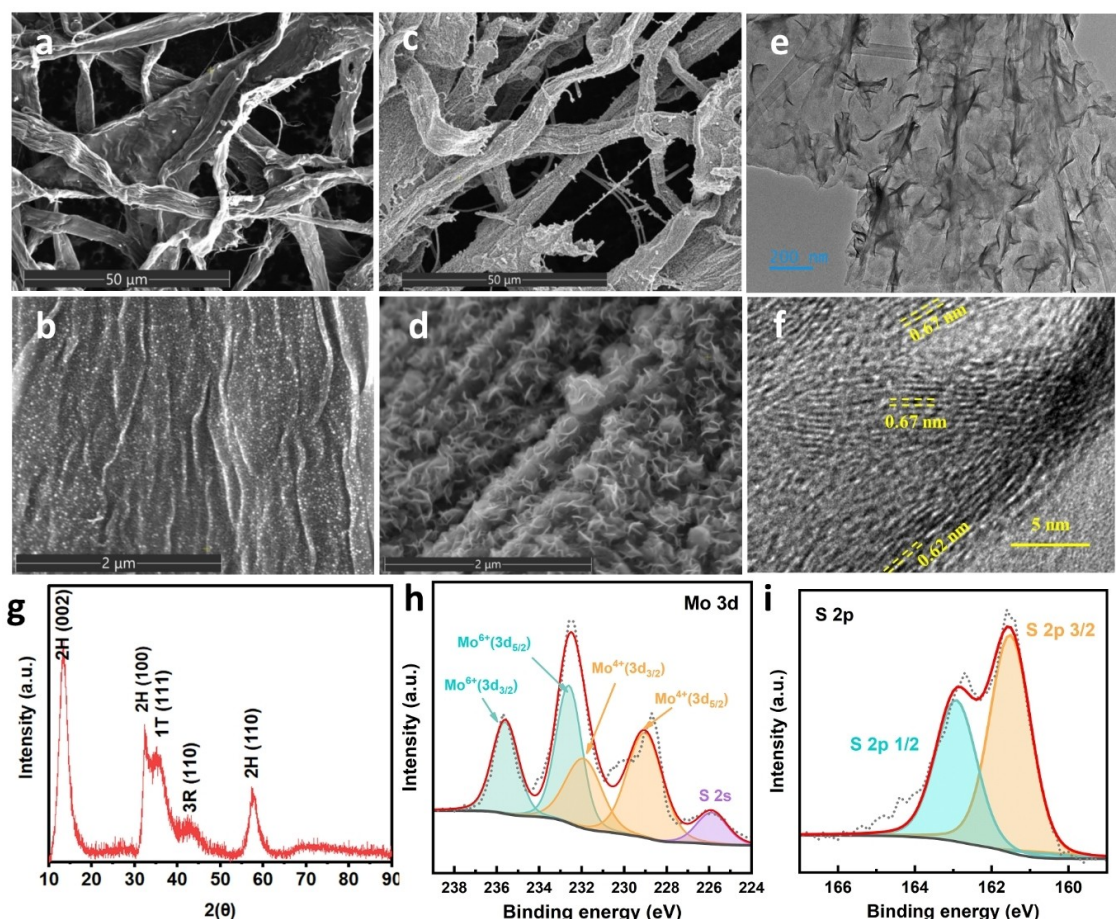


Figure 1. Schematic of the VOM-CC electrode fabrication process.



**Figure 2.** The SEM micrographs of a, b) CC and c, d)VOM-CC-2h. e, f) TEM micrographs, g) XRD pattern, XPS spectra of h) Mo 3d and i) S 2p for VOM-CC-2h sample.

dense and ball-like cluster features further appeared which were overgrown on the underlying  $\text{MoS}_2$  nanoflakes (Figure S2). The increased nanoflake density and ball-like cluster formation certainly increases the  $\text{MoS}_2$  mass loading and its surface area, however, the nanoflake surface now becomes difficult to access, limiting the frequency response of fabricated ECs. Therefore, they are not a favorable morphology for HF-ECs studied in this work.

The transmission electron microscopy (TEM) imaging was also conducted to reveal the microscopic and layered structure of  $\text{MoS}_2$  nanoflakes for CC-VOM-2h. The vertical nanoflake feature can be more clearly observed in Figure 2(e). The high-resolution TEM image (Figure 2f) reveals the layered structure of  $\text{MoS}_2$  nanoflakes. Each flake was formed by multiple atomic layers, and the flake thickness is in the range of few nm to a maximum  $\sim 10\text{nm}$ . The lattice spacing between atomic layers was found to be between 0.61 nm to 0.67 nm, corresponding to the d-spacing of the (002) plane of 2H- $\text{MoS}_2$  with a standard 0.61 nm value. The slightly expanded interlayer distance might be caused by  $\text{Na}^+$  intercalation during the synthesis.

As can be appreciated, the freestanding VOM-CC electrode combines several unique features together, very suitable for developing HF-ECs. The oriented  $\text{MoS}_2$  nanoflakes provide easily accessible atomic edges. Just like graphene, these atomic edges

or steps have rich adsorption sites for electrolyte ions, and therefore, offer much higher charge storage capacity than its basal plane. The vertical orientation of  $\text{MoS}_2$  flakes, with sub- $\mu\text{m}$  flake height and wide opening network, minimizes the porosity effect which otherwise would restrict ionic transport and hence the high frequency response. The 3-D carbon fiber network offers a conductive interconnection between  $\text{MoS}_2$  flakes to reduce the electrode resistance and provide a large surface area on a given footprint for  $\text{MoS}_2$  deposition. Therefore, a large areal capacitance could be achieved.

The crystalline quality of the  $\text{MoS}_2$  nanoflakes was further analyzed with x-ray diffractometry (XRD), as shown in Figure 2(g). The (013) peak at  $39.5^\circ$  and the (015) peaks at  $49.8^\circ$  which are the characteristic peaks for bulk  $\text{MoS}_2$  are not observed which clearly represent the formation of layered  $\text{MoS}_2$ .<sup>[14]</sup> The peaks at  $13.4^\circ$ ,  $32.3^\circ$  and  $57.3^\circ$  can be referred to (002), (100) and (110) planes of 2H- $\text{MoS}_2$  respectively (JCPDS card no.: 00-024-0513). In addition to this, (111) plane corresponding to 1T- $\text{MoS}_2$  is also observed at  $35.0^\circ$  and hence the coexistence of 2H and 1T phase of  $\text{MoS}_2$  is inferred, i.e., 1T/2H- $\text{MoS}_2$ .<sup>[15]</sup> In 1T- $\text{MoS}_2$  phase, the partially filled  $d_{xy}/d_{yz}/d_{zx}$  degenerate orbitals provide metallic property to the material. The high electrical conductivity ( $10\text{--}100 \text{ Scm}^{-1}$ ) and hydrophilicity of the 1T  $\text{MoS}_2$  phase contribute to the high

supercapacitive performance of 1T-MoS<sub>2</sub> electrode.<sup>[16]</sup> The large anionic polarizability of S<sup>2-</sup> due to their large ionic size which in turn leads to high ionic diffusivity in TMDCs is another factor positively impacting their pseudocapacitive performance. The d-spacing of 2H-MoS<sub>2</sub> for the (002) plane ( $2\theta=13.4^\circ$ ) was also observed to be expanded to 0.66 nm due to the Na<sup>+</sup> intercalation.<sup>[15b,17]</sup> The coexistence of 1H and 2T structures causes a crystal strain inside the lattice which favorably activates the inert basal planes towards electrocatalytic activity allowing easier and efficient intercalation/deintercalation of cations from the electrolyte into the MoS<sub>2</sub> crystal.<sup>[18]</sup> This allows faradic reactions to occur at very high rate at the electrode-electrolyte interface and therefore high capacitance values at high frequency may be expected from 1T/2H-MoS<sub>2</sub> nanoflakes. In addition, a tiny peak at 42.5° may be characteristic of small amounts of 3R-MoS<sub>2</sub> formed during the synthesis process and corresponds to its (015) plane. The phase information was further characterized by Raman spectroscopy (Figure S3).

X-ray photoelectron spectroscopy (XPS) was utilized to investigate the chemical composition and oxidation states of elements in MoS<sub>2</sub> nanocomposites. The XPS wide survey analysis (Figure S4) confirms the presence of Mo and S on the carbon surface. The atomic percentage (at%) of Mo was determined to be 15.45 at% for VOM-CC-2h5 m, higher than the 9.74 at% for VOM-CC-2h, indicating an increased loading of MoS<sub>2</sub> with longer growth time. To measure the binding energies of Mo and S atoms, high-resolution XPS analysis was conducted. There exist three distinct Mo 3d peaks at 229.1, 232.2, and 235.9 eV (Figure 2h), which were further deconvoluted into two separate overlapping doublets. The first doublet peaks, appearing at lower binding energy (228.8 eV and 231.8 eV), were attributed to the 4+ oxidation state of Mo, corresponding to Mo<sup>4+</sup> (3d<sub>5/2</sub>) and Mo<sup>4+</sup> (3d<sub>3/2</sub>), with an electron spin-orbit splitting of 3.1 eV.<sup>[19]</sup> Meanwhile, the second doublet peaks observed at higher binding energy (232.3 eV and 235.9 eV) were attributed to the Mo (6+) oxidation state, corresponding to Mo<sup>6+</sup> (3d<sub>5/2</sub>) and Mo<sup>6+</sup> (3d<sub>3/2</sub>), respectively.<sup>[20]</sup> This indicates a certain degree of oxidation occurring on the sample surface. Additionally, a small S 2 s peak was observed at 226.2 eV. The deconvolution of the S 2p spectra shown in Figure 2(i) revealed a S 2p 3/2 peak at 161.9 eV and a S 2p 1/2 peak at 163.1 eV, exhibiting a spin-orbit splitting ratio closer to 2:3 rather than the 1:2 ratio characteristic of elemental sulfur. This finding further supports the existence of the S<sup>2-</sup> oxidation state in the 2 h-MoS<sub>2</sub> composite.<sup>[21]</sup> These results are in good agreement with reported data for MoS<sub>2</sub> materials.<sup>[22]</sup> In the case of the COM-CC-2hm sample, the intensity of Mo<sup>6+</sup> peaks slightly decreased, while the signal of Mo<sup>4+</sup> peaks increased with longer deposition time. The suppression of the Mo<sup>6+</sup> peak indicates that the Mo<sup>6+</sup> peaks primarily originated from the surface oxidation of MoS<sub>2</sub>.<sup>[23]</sup>

### Aqueous HF-ECs

Based on its open morphology and highly ion-accessible nanostructure, VOM-CC-2h was tested as the electrode for

fabrication of HF-ECs. Cells with a symmetric two-electrode configuration were assembled inside coin cells with 6 M KOH as the aqueous electrolyte. Electrochemical impedance spectroscopy (EIS) and cyclic voltammetry (CV) were conducted to evaluate the performance of the devices.

In the Nyquist impedance plot (Figure 3a), both CC and VOM-CC based cells exhibit nearly vertical impedance spectra at low frequency range, behavior of a nearly ideal capacitor (a constant phase element with an ideality factor  $n=1$ ) connected in series with a resistance or an equivalent series resistance (ESR), suggesting they can be approximately modelled as a simple RC circuit. From the inset expanded view in the high frequency range, the difference between the two cells can be identified. The CC cell maintains its nearly vertical spectrum characteristic, but VOM-CC cell shows a tiny semicircle feature, which is most likely caused by a rapid pseudocapacitive effect (and hence a small charge transfer resistance) on layered MoS<sub>2</sub> surface or by a small interfacial resistance between the electrode material and the current collector. This feature in our cell does not occur until a high frequency, defined as the knee frequency, which was measured to be ~8.6 kHz. Therefore, the EIS spectrum of the VOM-CC cell can be modelled as a simple RC circuit below this frequency.

The Bode plots of the EIS spectra are shown in Figure 3(b). The areal capacitance of the whole cell was derived from EIS using:

$$C_A = \frac{-1}{2\pi f \times Z''(f) \times A} \quad (1)$$

where A is the single electrode area. The capacitance is plotted in Figure 3(c). The CC cell exhibits an absolute phase angle ( $\phi$ ) more than 80° at a few kHz frequencies, but this angle decreases as the frequency is reduced. This phenomenon was caused by the micropores formed in the carbon fibers during the carbonization process, as confirmed by the enlarged capacitance at low frequencies (Figure 3c). The rapid carbonization process can largely reduce the micropore density and volume but cannot eliminate them. In contrast, the absolute phase angle of VOM-CC at low frequencies is better than CC. This is because the deposited VOM on CC can block those micropores in CC. An absolute phase angle of ~80° was obtained at 120 Hz for the VOM-CC cell. The -45° phase angle frequency ( $f_0$ ) is found to be 4 kHz for the VOM-CC cell, as compared to 50 kHz observed for the CC cell.  $f_0$  is one useful parameter in evaluating the frequency response of HF-ECs. Neglecting the parasitic inductance in the low frequency range, the impedance ( $Z$ ) of a capacitor is determined by its parasitic resistance ( $R$ ) and capacitance ( $C$ ) as  $Z = R - j1/2\pi f C$ . At  $f_0 = 1/2\pi R C$ , the impedance phase angle reaches -45° with the same resistance and reactance values for the capacitor, while above this frequency, the resistance will dominate over the reactance and the cell behaves as a highly loss capacitor.  $f_0$  is reduced in the case of VOM-CC with growth of the VOM nanostructure; however, VOM nanostructure dramatically increases the areal capacitance density ( $C_A$ ) of the cell. A large capacitance of 0.8 mF/cm<sup>2</sup> at 120 Hz and 0.65 mF/cm<sup>2</sup> at 1 kHz

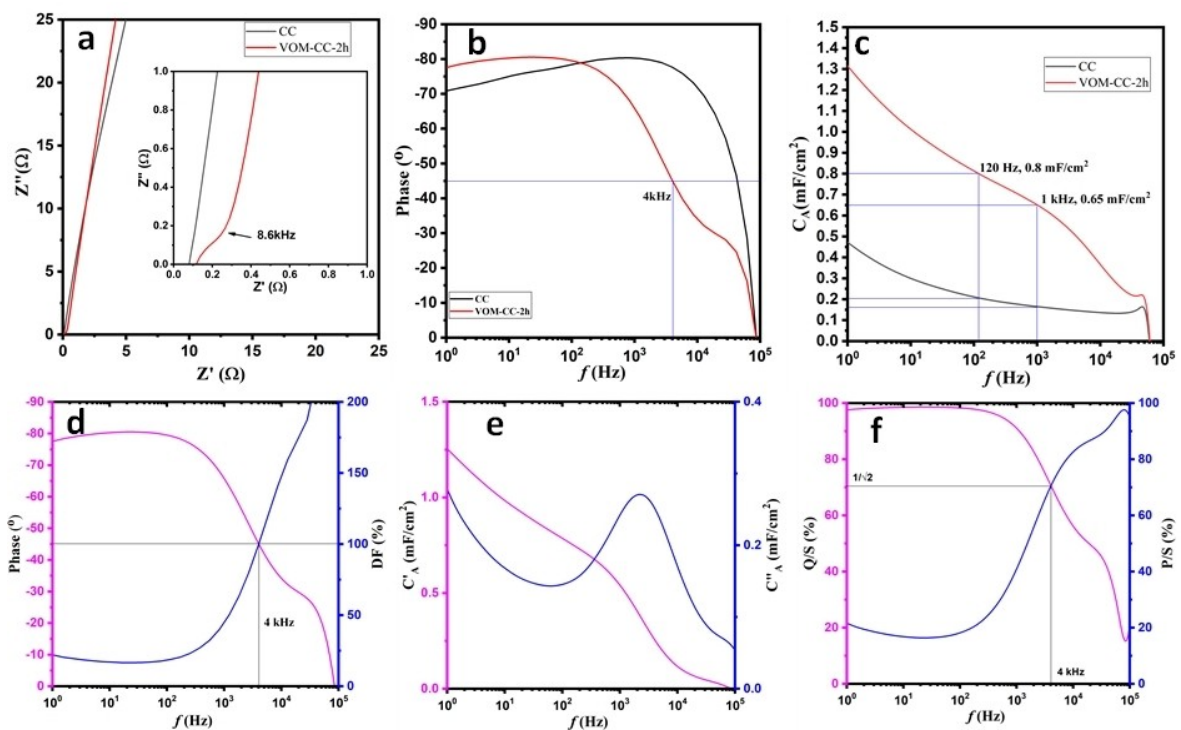


**Figure 3.** EIS spectra of CC cell and VOM-CC-2h cell in a) Nyquist plot, b) Bode plot, and c) the derived areal capacitance density for the cell. The frequency dependence of the VOM-CC-2h cell in terms of d) DF, e) complex capacitance, and f) Q/S and P/S.

were obtained for the VOM-CC-2h electrode-based cell, in compared to the  $0.2 \text{ mF/cm}^2$  at 120 Hz and  $0.15 \text{ mF/cm}^2$  at 1 kHz for the CC cell. The capacitance densities reported here, from electrodes fabricated in a facile process, are aligned with the state-of-the-art that commonly involves a complex fabrication process.

For a practical filtering capacitor, loss tangent ( $\tan\delta = Z''/|Z'|$ ) and the corresponding dissipation factor ( $DF = \tan\delta \times 100\%$ ) are crucial parameters evaluating the ratio of resistive power over reactive power of the capacitor, which ideally should have a small value in high-power applications. As shown in Figure 3(d), up to  $\sim 500$  Hz, the VOM-CC cell has a DF below 25%. It reaches 100% at  $f_0 = 4 \text{ kHz}$  when the resistive impedance equals the capacitive impedance. Above  $f_0$  ( $f_0 = 1/2\pi RC$ ), the resistive impedance is more than the capacitive impedance, and the cell behaves as a highly loss capacitor. The phase angle is negative until a frequency  $f_{max} = 1/2\pi\sqrt{LC}$ , where  $L$  is the parasitic inductance of the cell at this frequency. Above  $f_{max}$ , the cell will behave as an inductor, not a capacitor anymore. In the case of the VOM-CC-2h cell,  $f_{max} \sim 80 \text{ kHz}$ . Therefore, between  $f_0 = 4 \text{ kHz}$  and  $f_{max} \sim 80 \text{ kHz}$ , this cell could still be used as a filtering capacitor, although its DF will be much larger in this high frequency range.

The concept of a complex capacitance can be introduced for further analysis of an EC with resistive losses, which is defined as:

$$C_c(\omega) = C'(\omega) - jC''(\omega) = \frac{1}{j\omega Z} = \frac{-Z'' - jZ'}{\omega|Z|^2} \quad (2)$$

And hence

$$C(\omega) = \frac{-Z''}{\omega|Z|^2} = -\frac{\sin\phi}{\omega|Z|} \quad C''(\omega) = \frac{Z'}{\omega|Z|^2} = \frac{\cos\phi}{\omega|Z|} \quad (3)$$

where  $\phi$  is the phase angle of the impedance,  $C'(\omega)$  is the capacitance, and  $C''(\omega)$  is associated with energy dissipation due to internal loss. In the case of an ideal blocking electrode-based EC with a capacitance  $C$  and a resistance  $R$ , its complex capacitance is:

$$C(\omega) = \frac{C}{1 + (\omega RC)^2} \quad C''(\omega) = \frac{\omega RC^2}{1 + (\omega RC)^2} \quad (4)$$

Where  $C'$  arrives its resonant maximum at the characteristic frequency  $f_0$ , and at this frequency,  $C'(f_0) = C/2$ .

In Figure 3(e), we analyzed our VOM-CC-2h cell based on the complex capacitance. The derived capacitance  $C'_A$  has a value very close to the capacitance in Figure 3(c). A resonant frequency of  $\sim 2.5 \text{ kHz}$  was found, which is also close to the  $f_0 = 4 \text{ kHz}$  derived from Figure 3(b). The difference is caused by the non-ideal blocking electrode property of VOM-CC electrodes.

Treating the nonideal EC as a load powered by a sinusoidal source  $V(\omega)$  with an amplitude of  $V_m$ , the real power  $P$ , the reactive power  $Q$ , and the apparent power  $S$  can be derived from the complex power  $S$ , defined as:

$$S = P + jQ = \frac{1}{2}VI^* \quad (5)$$

With  $V$  and  $I$  are the voltage and current phasors, respectively. From impedance definition,  $Z = \frac{V}{I} = \frac{V_m}{I_m} e^{j\varphi} = |Z|e^{j\varphi}$ , we have

$$S = \frac{V_m^2}{2|Z|} e^{j\varphi} = \frac{V_m^2}{2|Z|} \cos\varphi + j \frac{V_m^2}{2|Z|} \sin\varphi \quad (6)$$

and hence,

$$P = \frac{V_m^2}{2|Z|} \cos\varphi = \frac{V_m^2}{2} \omega C'' \quad (7)$$

$$Q = \frac{V_m^2}{2|Z|} \sin\varphi = -\frac{V_m^2}{2} \omega C' \quad (8)$$

$$S = \frac{V_m^2}{2|Z|} \quad (9)$$

For a HF-EC, since its capacitance dominates at low frequencies and resistance dominates at high frequencies, the normalized power  $P/S$  and the normalized reactive power  $|Q|/S$  will have a value between 0 and 1. When these two normalized powers equal,  $\varphi=45^\circ$  and the normalized power will be  $1/\sqrt{2}$ . It is further noticed that the dissipation factor:

$$DF = \frac{P}{|Q|} \times 100\% = \frac{C''}{C'} \times 100\% \quad (10)$$

In Figure 3(f),  $P/S$  and  $|Q|/S$  are plotted against the frequency, and again,  $f_0$  of 4 kHz at  $\varphi=45^\circ$  was derived. Since the ratio of  $P/S$  and  $|Q|/S$  is DF, or  $C''/C'$ , at the cross point of the two curves  $C''=C'$ , or from Equation (4),  $f = 1/2\pi RC$ , which gives the  $-45^\circ$  phase angle frequency.

Long-term cycling stability is another parameter of filtering ECs. Galvanostatic charge-discharge tests were conducted under a high current density of  $10\text{mAcm}^{-2}$  after the freshly-made cell was stabilized to passivate the surface-related reactions. The cell capacitance retention, coulombic efficiency, and charge/discharge profile are shown in Figure S6. After surface passivation, the capacitance exhibited high stability and

remained almost constant. After the  $1\times10^6$  fully charging-discharging cycles, the capacitance retention was above 98% of the initial value. The outstanding cycling stability of our VOM-CC freestanding electrodes confirms the chemical and structural stability of  $\text{MoS}_2$  nanosheets and CC scaffold, as well as the strong bonding between them.

We further tested the EC cell performance based on a set of VOM-CC samples which were prepared by varying  $\text{MoS}_2$  hydrothermal growth times of 2 h, 2 h 5 m, 2 h 15 m, and 3 h. Their complex impedance Nyquist plot is shown in Figure 4(a). As more  $\text{MoS}_2$  nanoflakes were deposited, the porous effect and the interface resistance effect became more significant, giving rise to the more obvious Warburg region and semicircle features that caused a slower frequency response. From the phase plot (Figure 4b), we can see a progressive decrease in the frequency response of the electrode with increased deposition time. The cells based on the four samples exhibited 120 Hz phase angle of  $-79.5^\circ$ ,  $-69.5^\circ$ ,  $-35.0^\circ$ , and  $-12.5^\circ$ , and the characteristic frequency at  $-45^\circ$  phase angle of 4k, 600, 60, and 7 Hz, respectively. The cell areal capacitance is plotted in Figure 4(c). At 1 Hz, VOM-CC-3 h cell has a capacitance of  $\sim 210\text{mF/cm}^2$ . In particular, the VOM-CC-2h5 m cell exhibits a 120 Hz phase angle of  $-69.5^\circ$  and a remarkable capacitance of  $4.8\text{mF/cm}^2$ . Such a capacitor, with a lower frequency response but higher capacitance density, is suitable for pulse power applications at a low repetition rate.

### Organic HF-ECs

The VOM-CC electrodes were also tested in organic electrolyte cells using 1 M TEABF<sub>4</sub> in acetonitrile as the electrolyte. The operable voltage window of an aqueous cell is restricted to below 0.8 V, while TEABF<sub>4</sub>/ACN has a wide voltage window of 2.5 V. CV and EIS tests were conducted to evaluate the performance of VOM-CC-2h and VOM-CC-2h10 m based cells.

CV curves were acquired from 0 V to 2.5 V for a range of scan rates from 1 V/s to 50 V/s (Figure S7). In Figure 5(a), the CV curve is plotted at 50 V/s for comparison. The rectangular nature of the CV profile was maintained at 50 V/s even for the VOM-CC-2h10 m cell. For these two cells the calculated cell capacitance at 50 V/s is 0.4 and  $3.3\text{mF/cm}^2$ , respectively. The EIS derived plots are shown in Figure 5(b and c). Admittedly,

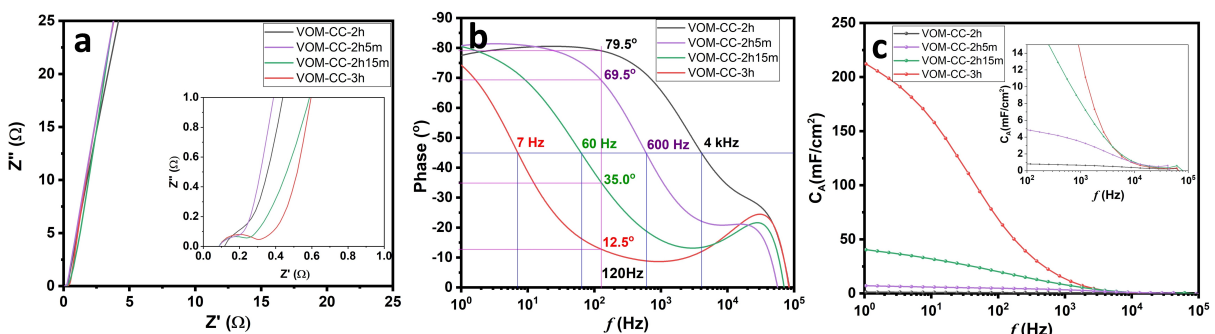
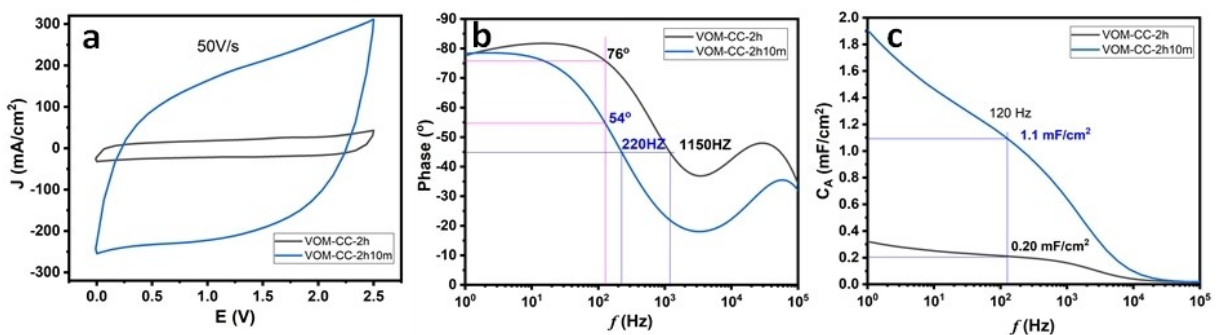


Figure 4. EIS spectra of a set of VOM-CC samples in a) Nyquist plot and b) Bode plot, and c) the derived cell capacitance density.



**Figure 5.** a) CV curves at a scan rate of 50 V/s, b) phase angle plot, and c) the derived capacitance of VOM-CC-2h and VOM-CC-2h10m based organic cells.

their capacitance ( $0.20 \text{ mF/cm}^2$ ,  $76^\circ$ , and  $1.2 \text{ mF/cm}^2$ ,  $54^\circ$  at  $120 \text{ Hz}$ ) and frequency response ( $f_o = 1150, 220 \text{ Hz}$ ) are lower than that of the corresponding aqueous electrolyte cells. This loss in frequency response was caused by the reduced ion diffusion and migration rates because of bulkier ions with larger inertia for  $\text{TEABF}_4$ , while the larger ion size also restricts ion accessibility to the smaller pores, limiting the capacitance.

Even though these organic ECs have a slower frequency response than their aqueous counterparts, their speed is still much higher than conventional ECs. Since our freestanding electrode is thin ( $\sim 10 \mu\text{m}$ ), these organic ECs were expected to have both high energy and high power densities. For the VOM-CC-2h10 m cell, if we only consider the volume of the two electrodes, the calculated energy density and power density for this cell are  $0.36 \text{ mWh cm}^{-3}$  and  $26 \text{ Wcm}^{-3}$  at  $50 \text{ V/s}$ . This power density similar to AECs, but AECs have an energy density in the range of  $\mu\text{Wh cm}^{-3}$ , much smaller than our ECs. The energy and power densities calculated here imply that the VOM-CC based ECs can operate in practical cases where high energy storage and rapid release are needed.

### Ripple filtering demonstration

As proof of concept, we demonstrated the application of our kHz ECs for ripple filtering in AC/DC conversion. The full wave conversion circuit is shown in Figure 6(a), with D1–D4 as the diodes, C as the filtering capacitor and R the load. Figure 6(b) shows the input sinusoidal wave  $V_i$  with frequency  $f$  and the output  $V_o$  with a ripple voltage  $V_r$ , which is given by.<sup>[24]</sup>

$$V_r \approx \frac{V_0}{2fCR} \quad (11)$$

This equation indicates that for a given load  $R$ , the ripple voltage is inversely proportional to both  $f$  and  $C$ . Although the capacitance of an EC decreases with frequency, from Figure 3(e), the multiplication of  $fC$  in fact increases with frequency. Therefore, as long as the phase angle is still negative (or  $C > 0$ ), the ripple voltage will not increase. This suggests that at least for sinusoidal waves, up to its resonant frequency  $f_{\max}$  where the effective capacitance becomes null, the EC can be used for ripple filtering. For non-sinusoidal waves, the high

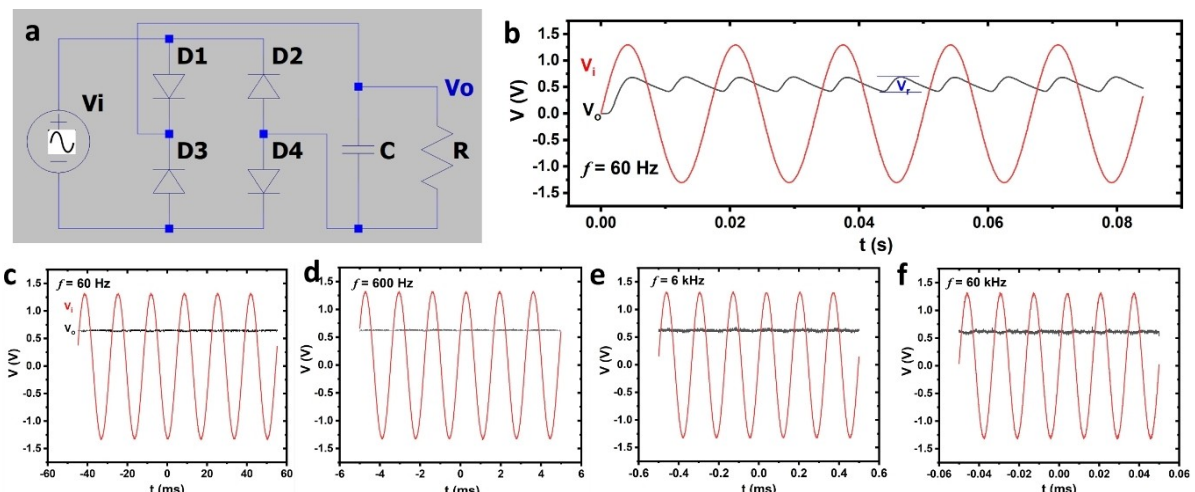


**Figure 6.** a) Schematic circuit of AC/DC full-wave conversion using an EC as the filtering capacitor. b) One simulation result of the regular ripple pattern. c–f) Measured load voltage after EC filtering for a sinusoidal input at different frequencies.

order harmonic components with frequencies above  $f_{\max}$  will enhance the ripple.

Figure 6(c–f) presents the filtered DC voltage on the load  $R$  (500 k $\Omega$ ) using our VOM-CC-2h based EC, with  $f_{\max} \sim 80$  kHz, for the input sinusoidal wave with a frequency from 60 Hz to 60 kHz. There is no obvious ripple component on the load. The observed noise most likely is associated with the measurement itself, but not with the ripple which has a regular pattern. Not shown here, when the frequency of the input wave is above 100 kHz, the EC loses its filtering function. Since EC has a large capacitance, to observe the ripple phenomenon, the load resistance must be very small, and the frequency is low. One example is presented in Figure S8.

## Conclusions

In summary, kilohertz electrochemical capacitors (ECs) were demonstrated using a freestanding composite electrode fabricated via a facile process. The electrode had a rapidly pyrolyzed cellulose sheet acted as a 3D scaffold, on which vertically oriented MoS<sub>2</sub> nanoflakes were deposited in a hydrothermal process. The amount of MoS<sub>2</sub> deposition had a significant impact on the capacitance density and the frequency response of the fabricated ECs. With an aqueous electrolyte, the ultrafast ECs exhibited a cell-level capacitance density of 0.8 mF/cm<sup>2</sup> at 120 Hz and 0.65 mF/cm<sup>2</sup> at 1 kHz and a frequency of 4 kHz at  $-45^\circ$  phase angle. Their excellent filtering capability was demonstrated up to a frequency of 60 kHz. ECs with a remarkable capacitance of 4.8 mF/cm<sup>2</sup> were also demonstrated with a 120 Hz phase angle of  $-69.5^\circ$ . Such a capacitor, with a lower frequency response but higher capacitance density, is suitable for pulse power applications. These results, combined with the simple electrode structure and its facile fabrication process, suggest that miniaturized ECs could substitute bulky AECs for ripple filtering and other applications.

## Experimental Section

Sodium molybdate(VI) dihydrate(99 + %) was obtained from ACROS Organics and thiourea(99 + %) was procured from Thermo Fisher Scientific. Kimwipe was obtained from KIMTECH brand. All materials were used as obtained without any purification.

Carbonized cellulose microfiber sheets were obtained by rapid pyrolysis of Kimwipe sheets. Briefly, the Kimwipe sheets were inserted into a tube furnace preheated at 1000 °C in an inert environment. The obtained black films were carbonized cellulose, labelled CC, on which vertically oriented MoS<sub>2</sub> nanoflakes were further grown. For the growth of MoS<sub>2</sub>, 0.5 g Sodium molybdate dihydrate and 0.75 g of thiourea were dissolved in 30 ml deionized (DI) water. The solution was loaded into a Teflon-lined autoclave. The reaction was carried out at 220 °C for 2 h followed by 6 h of cooldown. The contents of the autoclave were carefully removed, and the film was washed three times with DI water and two times with ethanol. The film was dried on a hot plate at 60 °C for 30 minutes before heating inside a vacuum oven overnight at 80 °C. The obtained film electrode is vertically oriented MoS<sub>2</sub> nanoflakes on carbonized cellulose microfibers, abbreviated VOM-CC-2h.

Reactions were also carried out for a reaction time of 2 h 5 min, 2 hr 10 min, 2 h 15 min, 2 hr 30 min, and 3 hr. The obtained film electrodes were abbreviated as VOM-CC-2h5 m, VOM-CC-2h10 m, VOM-CC-2h15 m and similarly for the rest.

Microscopic imaging for analyzing the morphology and crystalline structure of VOM-CC films was accomplished using a Helios 5 UX scanning electron microscope (SEM) and a JEOL 2010F transmission electron microscope (TEM). X-ray diffraction analysis was conducted using Cu  $K_\alpha$  radiation ( $\lambda = 0.1541$  nm) on an X-ray Diffractometer (Malvern PANalytical Aeris). X-ray photoelectron spectroscopy (XPS) data were acquired using a spectrometer (Kratos Axis Supra + apparatus). The photoelectrons were excited by monochromatic Al  $K_\alpha$  radiation ( $h\nu = 1486.6$  eV), and the high-resolution spectra were acquired with a step of 0.1 eV and the pass energy of 23.5 eV. To correct for sample charging, the binding energy (BE) of spectra was referenced to the adventitious carbon C 1s BE at 284.8 eV.

To analyze the electrode performance, 2016-type coin cells with symmetric electrodes were assembled using either 6 M KOH as the aqueous electrolyte or 1 M TEABF<sub>4</sub> in acetonitrile as the organic electrolyte. The electrode has a mass density of 1.6 mg cm<sup>-2</sup>. The electrode area is 0.5 × 0.5 cm<sup>2</sup>. Electrochemical measurements were conducted using a Biologic SP-250 electrochemical workstation. Electrochemical impedance spectroscopy (EIS) was measured from 100 kHz to 0.1 Hz with a sinusoidal ac voltage of 10 mV amplitude. Cyclic voltammetry (CV) was carried out in the 0–0.8 V range for aqueous cells, and the 0–2.5 V range for organic electrolyte cells.

## Acknowledgements

This work is supported by the National Science Foundation under Grant 2122921. We acknowledge the use of facilities within the Eyring Materials Center at Arizona State University, supported in part by NNCI-ECCS-2025490.

## Conflict of Interests

The authors declare no conflict of interest.

## Data Availability Statement

The data that support the findings of this study are available from the corresponding author upon reasonable request.

**Keywords:** ultrafast electrochemical capacitors • AC filtering • pulse power • MoS<sub>2</sub> • cellulose

- [1] a) J. R. Miller, R. Outlaw, B. Holloway, *Science* **2010**, *329*, 1637; b) Z. Fan, N. Islam, S. B. Bayne, *Nano Energy* **2017**, *39*, 306; c) J. Park, W. Kim, *Adv. Energy Mater.* **2021**, *11*, 2003306; d) J. R. Miller, R. A. Outlaw, *J. Electrochem. Soc.* **2015**, *162*, A5077.
- [2] a) N. Islam, S. Li, G. Ren, Y. Zu, J. Warzywoda, S. Wang, Z. Fan, *Nano Energy* **2017**, *40*, 107; b) M. Wu, K. Sun, J. He, Q. Huang, W. Zhan, Z. Lu, M. C. Xia, Y. Zhang, X. Lyu, H. Geng, *Adv. Funct. Mater.* **2023**, *23*05039; c) S. Fang, G. Miao, K. Chen, J. Xing, S. Zhou, Z. Yang, W.-H. Liao, *Energy* **2022**, *241*, 122833; d) S. Fang, N. Padar, M. J. Mirzaei, S. Zhou, W.-H. Liao, *Acta Mech. Sin.* **2022**, *38*, 521535; e) S. A. Kouritem, M. A. Bani-Hani, M. Beshir, M. M. Elshabasy, W. A. Altabay, *Energies* **2022**, *15*, 7271.

- [3] P. Xue, K. Zhu, W. Gong, J. Pu, X. Li, C. Guo, L. Wu, R. Wang, H. Li, J. Sun, *Adv. Energy Mater.* **2022**, *12*, 2200308.
- [4] a) D. Zhao, K. Jiang, J. Li, X. Zhu, C. Ke, S. Han, E. Kymakis, X. Zhuang, *BMC Materials* **2020**, *2*, 1; b) M. Wu, F. Chi, H. Geng, H. Ma, M. Zhang, T. Gao, C. Li, L. Qu, *Nat. Commun.* **2019**, *10*, 2855.
- [5] S. Zhang, B. Li, C. Cui, W. Qian, Y. Jin, *Batteries & Supercaps* **2023**, *6*, e202200566.
- [6] Z. Li, L. Zhao, X. Zheng, P. Lin, X. Li, R. Li, D. Han, S. Zhao, D. Lv, L. Wang, *Chem. Eng. J.* **2022**, *430*, 133012.
- [7] F. Wang, Z. Guo, Z. Wang, H. Zhu, G. Zhao, C. Chen, M. Liu, R. Sun, F. Kang, C. P. Wong, *Adv. Mater.* **2023**, *35*, 2210038.
- [8] a) M. A. Bissett, S. D. Worrall, I. A. Kinloch, R. A. Dryfe, *Electrochim. Acta* **2016**, *201*, 30; b) A. De Adhikari, N. Shauloff, Y. Turkulets, I. Shalish, R. Jelinek, *Adv. Electron. Mater.* **2021**, *7*, 2100025; c) R. M. Tamgadge, S. Kumar, A. Shukla, *J. Power Sources* **2020**, *465*, 228242; d) A. Morag, N. Maman, N. Froumin, V. Ezersky, K. Rechav, R. Jelinek, *Adv. Electron. Mater.* **2020**, *6*, 1900844.
- [9] a) L. Wang, L. Zhao, M. Song, L. Xie, X. Wang, X. Li, Y. Huang, M. Wei, Q. Jin, X. Meng, *J. Energy Chem.* **2023**, *78*, 158; b) M. Zhang, K. Dong, S. Saeedi Garakani, A. Khorsand Kheirabad, I. Manke, M. Wu, H. Wang, L. Qu, J. Yuan, *Adv. Sci.* **2022**, *9*, 2105072; c) S. Xu, Y. Wen, Z. Chen, N. Ji, Z. Zou, M. Wu, L. Qu, J. Zhang, *Angew. Chem.* **2021**, *133*, 24710; d) Y.-F. Fan, Z.-L. Yi, G. Song, Z.-F. Wang, C.-J. Chen, L.-J. Xie, G.-H. Sun, F.-Y. Su, C.-M. Chen, *Carbon* **2021**, *185*, 630.
- [10] G. Ren, X. Pan, S. Bayne, Z. Fan, *Carbon* **2014**, *71*, 94.
- [11] J. Park, J. Lee, W. Kim, *ACS Energy Lett.* **2021**, *6*, 769.
- [12] F. Han, O. Qian, G. Meng, D. Lin, G. Chen, S. Zhang, Q. Pan, X. Zhang, X. Zhu, B. Wei, *Science* **2022**, *377*, 1004.
- [13] G. Ren, S. Li, Z.-X. Fan, M. N. F. Hoque, Z. Fan, *J. Power Sources* **2016**, *325*, 152.
- [14] C. D. Quilty, L. M. Housel, D. C. Bock, M. R. Dunkin, L. Wang, D. M. Lutz, A. Abraham, A. M. Bruck, E. S. Takeuchi, K. J. Takeuchi, *ACS Appl. Energ. Mater.* **2019**, *2*, 7635.
- [15] a) M. R. Saber, G. Khabiri, A. A. Maarouf, M. Ulbricht, A. S. Khalil, *RSC Adv.* **2018**, *8*, 26364; b) S. B. Saseendran, A. Ashok, A. Asha, *Int. J. Hydrogen Energy* **2022**, *47*, 9579.
- [16] M. Acerce, D. Voiry, M. Chhowalla, *Nat. Nanotechnol.* **2015**, *10*, 313.
- [17] K. Krishnamoorthy, G. K. Veerasubramani, S. Radhakrishnan, S. J. Kim, *Mater. Res. Bull.* **2014**, *50*, 499.
- [18] a) H. He, X. Li, D. Huang, J. Luan, S. Liu, W. K. Pang, D. Sun, Y. Tang, W. Zhou, L. He, *ACS Nano* **2021**, *15*, 8896; b) H. Li, C. Tsai, A. L. Koh, L. Cai, A. W. Contryman, A. H. Fragapane, J. Zhao, H. S. Han, H. C. Manoharan, F. Abild-Pedersen, *Nat. Mater.* **2016**, *15*, 48.
- [19] P. Qin, G. Fang, W. Ke, F. Cheng, Q. Zheng, J. Wan, H. Lei, X. Zhao, *J. Mater. Chem. A* **2014**, *2*, 2742.
- [20] Y. Qiao, X. Hu, Y. Liu, G. Liang, M. C. Croft, Y. Huang, *J. Mater. Chem. A* **2013**, *1*, 15128.
- [21] a) D. K. Nandi, S. Sahoo, S. Sinha, S. Yeo, H. Kim, R. N. Bulakhe, J. Heo, J.-J. Shim, S.-H. Kim, *ACS Appl. Mater. Interfaces* **2017**, *9*, 40252; b) T. Sun, Z. Li, X. Liu, L. Ma, J. Wang, S. Yang, *J. Power Sources* **2016**, *331*, 180.
- [22] C. Altavilla, M. Sarno, P. Ciambelli, *Chem. Mater.* **2011**, *23*, 3879.
- [23] S. Hussain, J. Singh, D. Vikraman, A. K. Singh, M. Z. Iqbal, M. F. Khan, P. Kumar, D.-C. Choi, W. Song, K.-S. An, *Sci. Rep.* **2016**, *6*, 30791.
- [24] W. Li, S. Azam, G. Dai, Z. Fan, *Energy Storage Mater.* **2020**, *32*, 30.

Manuscript received: August 21, 2023

Revised manuscript received: October 4, 2023

Accepted manuscript online: October 17, 2023

Version of record online: November 6, 2023